

Uncovering the atomic structure of substitutional platinum dopants in MoS₂ with single-sideband ptychography

David Lamprecht,^{*,†,‡} Anna Benzer,[†] Manuel Längle,[‡] Mate Capin,[†] Clemens Mangler,[‡] Toma Susi,^{*,‡} Lado Filipovic,[†] and Jani Kotakoski^{*,‡}

[†]*Institute for Microelectronics, TU Wien, Gußhausstraße 25-29, 1040 Vienna, Austria*

[‡]*University of Vienna, Faculty of Physics, Boltzmannngasse 5, 1090 Vienna, Austria*

E-mail: lamprecht@iue.tuwien.ac.at; toma.susi@univie.ac.at; jani.kotakoski@univie.ac.at

Abstract

We substitute individual Pt atoms into monolayer MoS₂ and study the resulting atomic structures with single-sideband (SSB) ptychography supported by *ab initio* simulations. We demonstrate that while high-angle annular dark-field (HAADF) scanning transmission electron microscopy (STEM) imaging provides excellent *Z*-contrast, distinguishing some defect types such as single and double sulfur vacancies remains challenging due to their low relative contrast difference. However, SSB with its nearly linear *Z*-contrast and high phase sensitivity enables reliable identification of these defect configurations as well as various Pt dopant structures at significantly lower electron doses. Our findings uncover the precise atomic placement and highlight the potential of SSB ptychography for detailed structural analysis of dopant-modified 2D materials while minimizing beam-induced damage, offering new pathways for understanding and engineering atomic-scale features in 2D systems.

Introduction

Due to their high surface-to-volume ratio, 2D materials are promising candidates as active material for future catalytic and gas-sensing applications. Particularly MoS₂, which as a monolayer is an intrinsic direct band gap semiconductor, has attracted significant interest. However, a major limitation of MoS₂ as a catalytic material is the relative chemical inertness of its basal plane which severely restricts its potential use-cases. To overcome this problem, various material modification methods like surface metal decoration,^{1,2} defect-engineering,^{3,4} or the assembling of heterostructures with other 2D materials^{5,6} have been proposed and experimentally verified. Substitutional doping, where a single heteroatom replaces one or more atoms in the lattice, is considered a modification method of particular interest⁷ due to its simplicity and potentially high selectivity. Replacement of S atoms has been reported for over half of the elements on the periodic table,⁸ but atomic resolution confirmation of this incorporation remains scarce.

Substitution to chalcogene sites has been achieved either with direct incorporation during chemical vapor deposition (CVD) growth (e.g., O,⁹ Va¹⁰), alloying with other chalcogenes (e.g., Se¹¹), post-growth plasma implantation (e.g., N,¹² Cl¹³) or various hydrothermal methods (e.g., Rh,¹⁴ W¹⁵). Evidence for the substitution of Mo atoms is limited to bottom-up methods and mostly performed by adding metals to the precursor during CVD growth (e.g., Fe,¹⁶ Ta¹⁷) and hydrothermal growth methods (e.g., Pd¹⁸). Notably, there are few reports of implanting precious metals like Pt into MoS₂, despite various theoretical predictions regarding the potential of Pt-doped MoS₂ for gas-sensing and catalysis^{19,20}

In,²¹ Li et al. studied single Pt atoms on MoS₂ by separating individual atoms from clusters using the electron beam of an aberration-corrected scanning transmission electron microscope (STEM). They were able to successfully implant single Pt atoms into S vacancy sites and study their dynamics under the electron beam. However, their substitution method is barely scalable and not trivially adaptable to other elements or atomic sites. Several other studies have claimed selective substitution of Mo atoms with Pt^{19,22,23} atoms, but none have

provided atomic-resolution confirmation, which is essential to distinguish between true lattice incorporation and mere surface decoration.

In this study, we extend our previously published two-step implantation method, originally demonstrated for implanting graphene with Au,^{24,25} Fe, Ag, Ti²⁴ and Al^{24,26} to MoS₂. First, we introduce defects into monolayer MoS₂ using low-energy He ion irradiation with a plasma source. Subsequently we fill the vacancies with single Pt atoms stemming from an evaporation source. For structural analysis of the modified material, high-angle annular dark-field (HAADF)-STEM and simultaneous 4D-STEM imaging is carried out. The resulting 4D data stacks are used to reconstruct the phase information using the single-sideband (SSB) algorithm.²⁷

While in HAADF imaging the intensity of an individual atom scales in our imaging conditions with the atomic number Z ^{1,64,28} the phase contrast in ptychography is approximately linear to the amplitude of the projected potential Z ,²⁹ which results in an approximate linear dependence on Z for single atoms. This allows the simultaneous and precise imaging of neighboring heavy and light atoms with SSB, which is needed for the analysis of our structures.³⁰ Most importantly, we show that ptychography allows to reliably differentiate between Pt atoms trapped in V_{1S} and V_{2S} defects, a distinction that is challenging in HAADF-STEM due to their low contrast difference.

To obtain further insights into the observed structures, the vacancy-mediated substitution process is further explored using density functional theory (DFT). Overall, as our method relies on the filling of vacancies by adatoms, our results demonstrate a pathway for controlled substitutional doping of MoS₂ with arbitrary elements.

Results and discussion

CVD-grown MoS₂ samples were transferred from the SiO₂ substrate to Quantifoil Au TEM grids and subsequently introduced into a interconnected UHV system.³¹ The sample shows

large atomically clean areas with a low density of intrinsic defects when investigated with STEM. After initial imaging, the samples were transferred in UHV to the sample manipulation chamber and exposed to He ions with a kinetic energy of 171 ± 21 eV. The sample treatment is illustrated in Fig. 1, including atomic-resolution images at the different stages. Assuming a simple fully elastic knock-on event with a maximum energy transfer, a He ion needs a minimum kinetic energy of 130.2 eV to produce a Mo vacancy (V_{Mo}) due to the displacement threshold of ca. 20 eV³² of a Mo atom in MoS₂, and a minimum kinetic energy of 17.4 eV to produce a single S vacancy (V_{1S}) based on a displacement threshold of 6.9 eV.³³ Therefore the 170 eV ions should have enough energy to introduce defects into both sublattices.

After 10 min of ion irradiation with an estimated total fluence of 1.25×10^{13} cm⁻² the samples were transported under UHV to the microscope to image the defect structures. After imaging, Pt atoms were evaporated onto the sample using an e-beam evaporator, while keeping the sample under UHV. Nearly exactly the same sample area is shown in Fig. 1e before and in Fig. 1f after the evaporation. It is evident that Pt atoms are incorporated into the MoS₂ lattice, occupying the former V_{1S} , V_{2S} and V_{Mo} sites.

HAADF and SSB ptychography images of defect structures are shown in Fig. 2a together with corresponding image simulations conducted with *ab*TEM³⁴ based on relaxed atomic models. A comparison of the HAADF intensities of V_{1S} and V_{2S} and the pristine S₂ sites shows that it is difficult to differentiate between the pristine S sublattice and single S vacancies in HAADF imaging, requiring high doses and high magnification, which come with the disadvantage of introducing additional defects during the imaging process. Fortunately 4D-STEM ptychography has a much higher contrast and dose efficiency compared to HAADF images.³⁵ For 4D data collection, stacks with 512×512 real-space pixels were collected with a dwell time of 20 μ s and an average dose of ca. 1×10^5 e⁻/². The phase information was retrieved using the single-sideband (SSB) method with post-acquisition aberration correction as described in.²⁷

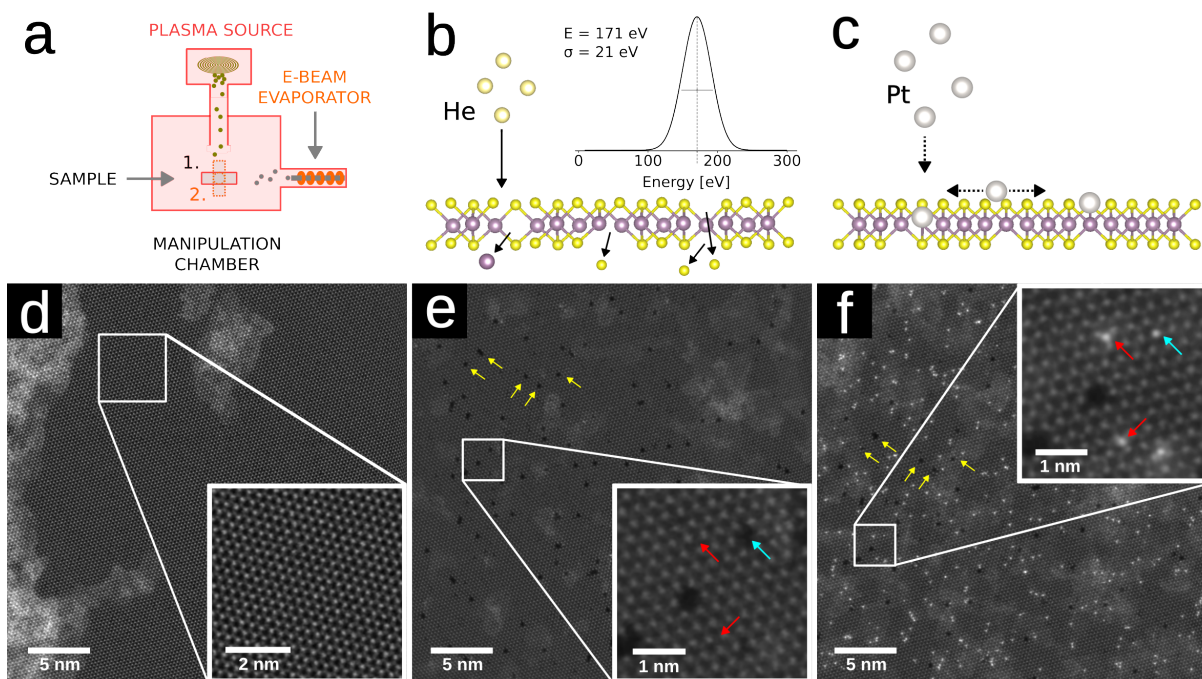


Figure 1: a) Schematic of the sample manipulation chamber used for the study. In step 1 the sample is subjected to the ion beam, in step 2 the sample is in the field of view of the e-beam evaporator. b) Schematic illustration of the defect-engineering process. The inset shows the beam energy profile of the He ions. (The full dI/dV curve can be found in Supplemental Materials Fig. S1.) c) Schematic illustration of the single atom evaporation process. d) HAADF-STEM image of a clean MoS₂ area before modification steps (not the same area as in the following images). e) HAADF-STEM image MoS₂ after 10 min irradiation with He ions. The red and turquoise arrows in the inset indicate V_{1S} (red) and V_{Mo} (turquoise) and defect sites that will be filled with Pt atoms, the yellow arrows mark the same defect features before and after Pt evaporation. f) HAADF-STEM image of roughly the same area and field-of-view as in e) (see yellow arrows); the sites filled with Pt atoms are indicated with the red and turquoise arrows in the inset.

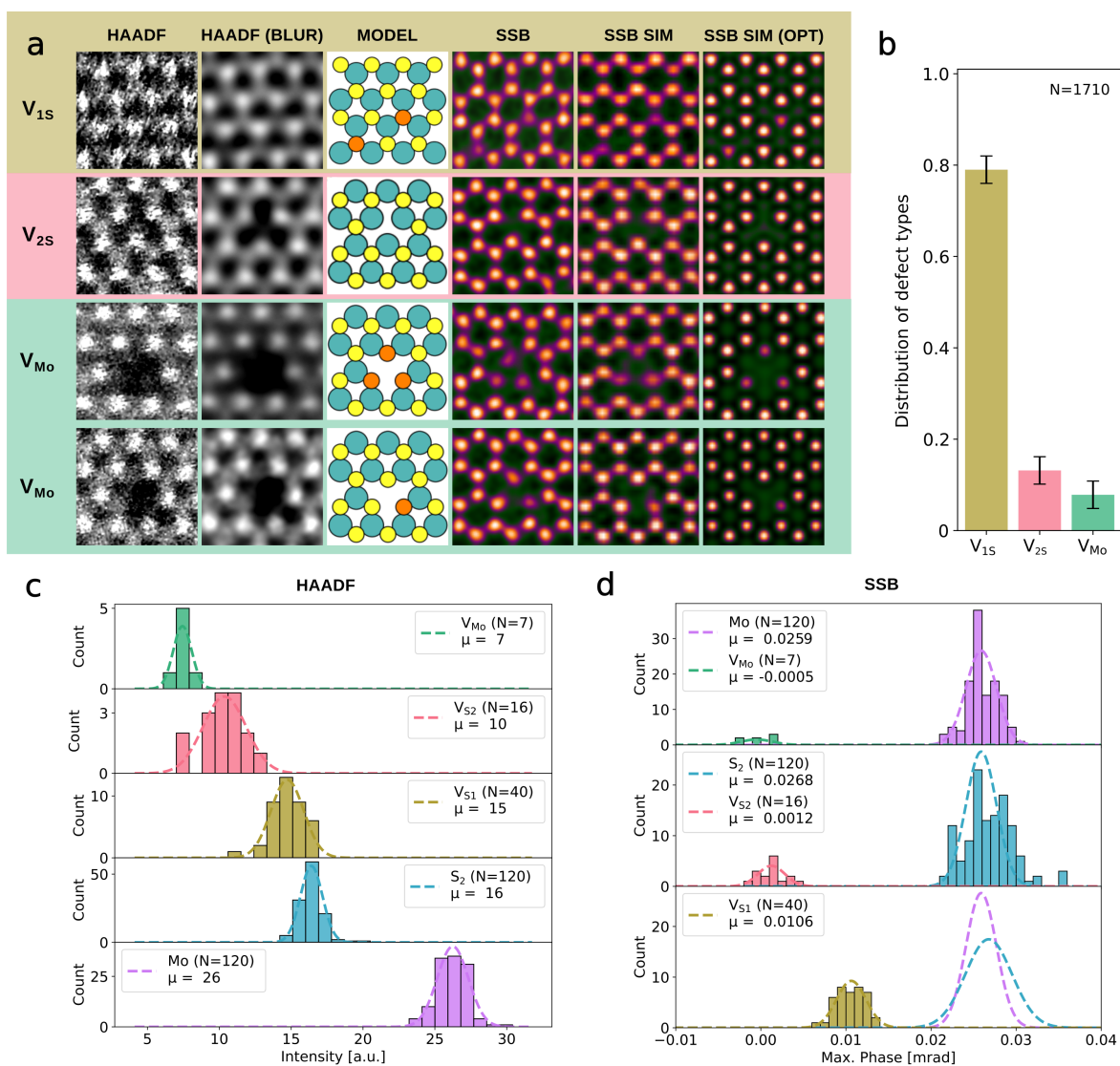


Figure 2: a) HAADF-STEM images (field of view ca. 1 nm) of defect structures without and with Gaussian blurring, atomic models of the imaged structures, SSB reconstructions of the phase information at the same location as well as simulations of the SSB images corresponding to experimental parameters. The last column contains simulations of the SSB images under perfect conditions (unlimited dose, no residual aberrations). b) Relative occurrence of different defect types in the defect-engineered MoS₂ based on SSB and HAADF images. The uncertainty in the columns is based on the variation between observed images. c) Histograms of HAADF intensities at the Mo and S₂ sublattice sites. The type of the S vacancies (no vacancy, V_{1S}, V_{2S}) are determined using the SSB intensity at the respective S sublattice site. d) Histograms of SSB phase values at the same atomic sites as in c), together with Gaussian fits of the phase distribution of all structures. *N* is the number of cases for each histogram.

The last two rows of Fig. 2a contain examples of defect clusters around a V_{Mo} site. While in the HAADF images, the neighborhood of the Mo vacancy is quite ambiguous and the number of neighboring S vacancies is hardly determinable, the SSB images clearly show a well-defined atomic structure. Mo-S vacancy structures with one to five missing sulfur atoms and a number of different vacancy configurations can be observed. Due to the relatively low ion fluence used in the experiments, the appearance of these vacancy structures are most likely due to a single impact and following collision cascades.

Figure 2b shows the ratio of the defect numbers derived from both large-scale HAADF imaging and small-scale phase reconstructions. Over 80 % of the introduced defects are $V_{1\text{S}}$, whereas $V_{2\text{S}}$ and V_{Mo} contribute with ca. 12 % and 8 % to the overall defect density of 1.3 ± 0.4 defects per nm^2 , in agreement to what we would expect at this ion energy.³⁶

Figure 2c-d contains histograms of the HAADF intensity and phase maxima at the same atomic positions in the defect-engineered MoS_2 as well as Gaussian fits of the distributions. The HAADF intensity distributions of pristine S_2 and the $V_{1\text{S}}$ overlap significantly and form a near-uniform distribution. By contrast, SSB images exhibit significantly larger phase ratios between the atomic columns enabling more precise defect identification. The mean peak of the $V_{1\text{S}}$ phase is located at $(10.9 \pm 1.9) \times 10^{-3}$ mrad and the mean peak of the S_2 at $(26.7 \pm 2.4) \times 10^{-3}$ mrad, which leads to an average intensity ratio of 2.6 between the two cases and allows for precise discrimination between defective and pristine sites in the sulfur sublattice.

The distributions of $V_{2\text{S}}$ and V_{Mo} are both centered around a phase of zero. Even though this seems to match optically with the simulated images, there is a significant difference visible in the line profiles of these structures in Supplementary Material Fig. S3. Unlike in HAADF imaging, the SSB phase displays a negative phase halo around a single atom which converges to the background value of zero phase after some distance.³⁷ In the case of MoS_2 , the negative halos of the six atomic columns around one hexagon nearly overlap, creating a deep phase trench with a small spike in the center of the hexagon. As only five of the

observed V_{2S} have a negative phase maximum we suspect that the sites are actually filled with light elements, which has already been discussed by Yin Wen.³⁸ Supplementary Material Fig. S3c-d contains image simulations and corresponding line profiles of V_{2S} doped with C and O, which are in a good agreement with the observed phase maxima at the supposed V_{2S} sites. Additional evidence stems from the fact that an unfilled V_{2S} would be subject to a lattice contraction of up to 12 %, ³⁹ which is not observed here. These substitutions are most likely C atoms from the hydrocarbon contamination which diffuse freely on the MoS_2 surface due to their low diffusion barriers (0.56 eV for C,⁴⁰ in comparison 1.92 eV for O⁴¹), before they fall into an energetically more favorable V_{2S} vacancy site (binding energy of 4.5 eV⁴⁰).

Even though similar reasoning could be applied to the observed phase maxima at V_{Mo} sites, the line profile analysis in Supplementary Material Fig. S4a-b shows that the center position of the V_{Mo} sites have a local maximum which is much lower than expected for V_{Mo} filled with a C atom in Fig. S4d. Therefore, the maximum values plotted in Fig. 2c originate from an overlap with the surrounding S atoms. A notable exception is shown in Supplementary Material Fig. S4c, where V_{Mo} is clearly filled with a heteroatom.

The negative halo effect on nearby atoms, together with distortions due to residual aberrations, scan distortions, the effect of light element adatoms and shot noise due to the limited dose,³⁵ is probably the main contributor to the observed phase variations of up to 3×10^{-3} mrad in all phase measurements. To account for this non-linearity, it is possible to quantify the phase directly with the contrast transfer function-based kernel developed by Hofer et al.³⁷ Using this method it is indeed possible to obtain quantitative phase contrast as we show in the phase quantification of an experimental image containing a V_{1S} (as well as $Pt@V_{1S}$) and the corresponding phase-image simulation, as can be seen in the Supplementary Material Fig. S6 and S7. Most importantly, the optimization provides a phase-contrast ratio between the average S_2 and V_{1S} columns of roughly 1.2, close to the ratio of 1.3 expected by the near linear Z -dependence of the phase contrast of single atoms. While this method is useful for

the analysis of ambiguous images, its use for large-scale statistical analysis is limited due to the need of an approximate atomic model.

Because the phase contrast of the Mo and S₂ sublattices have a ratio of only 1.03, simultaneous HAADF or virtual ADF images are required to determine the elemental composition of the material. While in HAADF images the presence of thin hydrocarbon contamination on the MoS₂ surface and at vacancy sites is indicated only by a low increase in background intensity, SSB reconstruction allows the visualization of individual carbon atoms in the vacancy sites and, to some degree, also on the MoS₂ surface (for an example see Supplementary Material Fig. S5).

As was already visible in Fig. 1f, after Pt evaporation, most Pt atoms occupy the sites of the sulfur sublattice. Some of these Pt atoms are unstable under the electron beam and jump to another sulfur site once the scan reaches their position (see Supplementary Material Fig. S8). These are most probably not adatoms on the pristine surface, as the energetically more favorable site for a Pt adatom is on top of a Mo site (see Fig. 3a). Further, the surface diffusion migration barriers for Pt are only between 0.4 and 0.6 eV (see Fig. 3a-b) depending on the location of the adatom, and thus the Pt atoms can easily diffuse over the MoS₂ surface until they fall into an energetically more favorable vacancy site. Therefore, we assume that the observed atom jumps take place between S vacancy sites, as described in Ref.²¹ The diffusion energy paths of Pt atoms into V_{1S}, V_{2S} and V_{Mo} vacancies are depicted in Fig. 3b-d and show binding energies of 2.6, 2.5 and 4.6 eV, respectively. All these binding energies are sufficient to ensure the stability of the implanted atom at room temperature.

Experimental and simulated HAADF and SSB images of the most typical Pt-doped sites are shown in Fig. 4a. As Pt atoms have a significantly higher nuclear charge ($Z = 78$) than the surrounding Mo ($Z = 42$) and S ($Z = 16$) atoms, the Pt atom in HAADF images appears as a large bright feature, obscuring the neighboring atomic structure. The contrast difference between a Pt atom located at a V_{2S} site (Pt@V_{2S}) with a theoretical Pt/Mo intensity ratio of 2.5 is very similar to Pt@V_{1S} with a theoretical (S+Pt)/Mo intensity ratio of 2.7. The

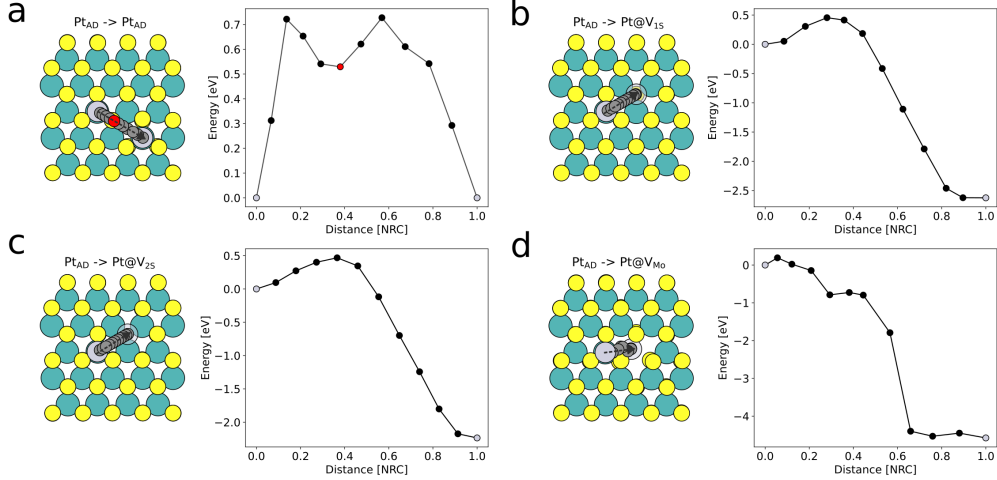


Figure 3: a-d) Diffusion paths of Pt atoms on the surface calculated by the nudged elastic band method. The x -axis in the energy diagrams are given in relative atomic mass-weighted distances (normalized reaction coordinates NRC). The black dots in the energy diagram match the (semi-transparent) gray circles on the atomic model. Start and end positions of the diffusion process are marked with silver dots. a) Diffusion from the top of a Mo site to the top of another Mo site over the metastable position on top of a S site (marked by the red dot). b) Diffusion from the surface to V_{1S} site, c) to a V_{2S} site and d) to a V_{Mo} site.

SSB images give a much clearer picture, with a Pt/Mo phase ratio obtained by simulations of 1.19 and a respective simulated (S+Pt)/Mo phase ratio of roughly 1.85. This is reflected in the experimental data, where we observed an average phase of $(43.4 \pm 2.1) \times 10^{-3}$ mrad for Pt@ V_{1S} , $(33.7 \pm 0.9) \times 10^{-3}$ mrad for Pt@ V_{1S} and $(33.8 \pm 1.6) \times 10^{-3}$ mrad for Pt@ V_{Mo} , which results in Pt/Mo and (S+Pt)/Mo ratios of 1.2 and 1.6, respectively. SSB imaging is also a powerful tool for analyzing Mo substitutions. Due to the considerably lower phase ratio of the Pt atom in comparison to the neighboring sites, discerning the neighborhood and exact placement of the Pt atom implanted in the defect clusters around V_{Mo} sites becomes significantly more straightforward, as can be seen in the third row of Fig. 4a.

Unfortunately the complex contrast formation in SSB may lead to misinterpretation of Pt adatoms located on top of the Mo sublattice, as can be seen in the fourth row of Fig. 4a, where HAADF imaging of this configuration provides significantly better contrast with a theoretical (Pt+Mo)/Mo intensity ratio of 5.6 compared to a Pt/Mo ratio of 2.5. As the observed adatoms are not kicked away by the electron beam, it is safe to assume that these

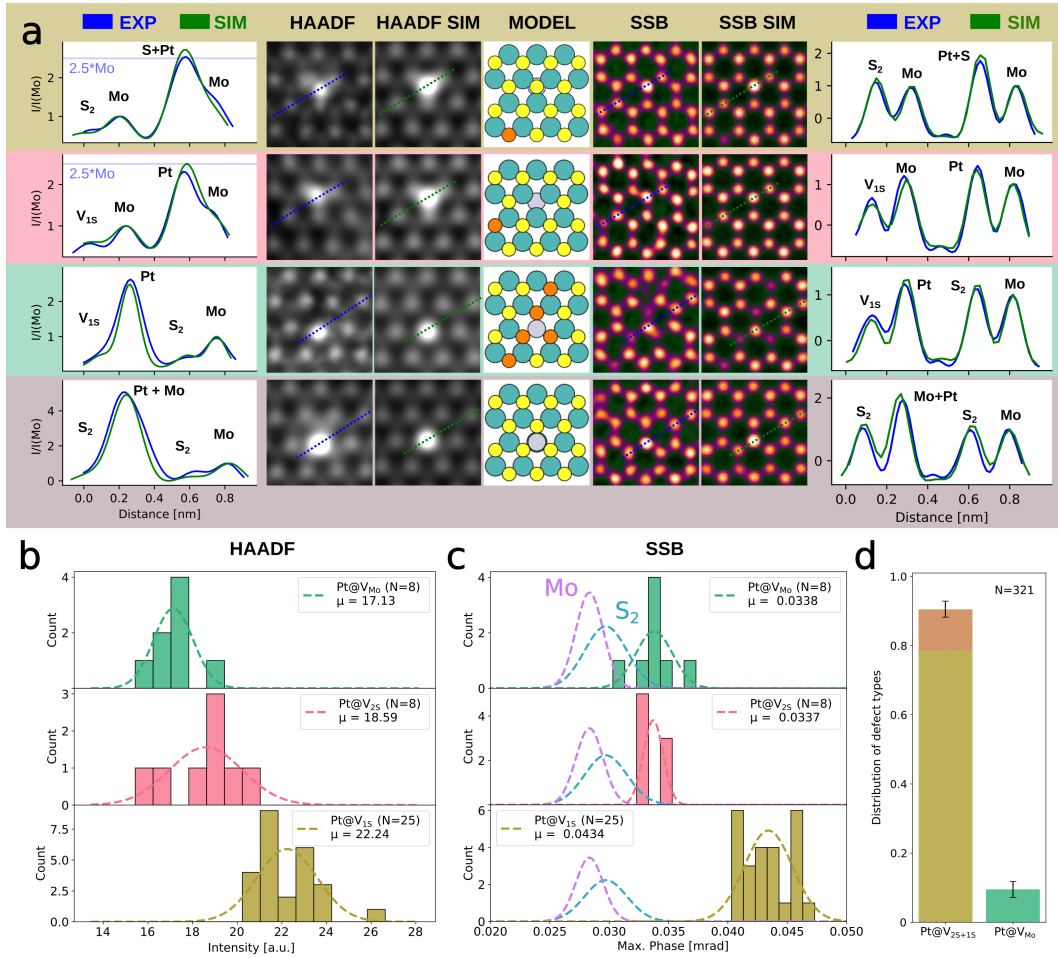


Figure 4: a) Line profiles of Gaussian blurred HAADF images of dopant structures, shown alongside the blurred images as well as HAADF simulations, atomic models of the imaged structures, SSB reconstructions of the phase information at the same location, and realistic simulations of the SSB images. The rows contain data of Pt@V_{1S}, Pt@V_{2S}, Pt@V_{Mo} and Pt adatom columns, respectively. b) Histograms of HAADF intensities at Pt@V_{1S}, Pt@V_{2S} and Pt@V_{Mo} sites and Gaussian fits of the distributions. The types of the Pt substitutions at the S₂ sublattice are determined using the SSB phase at the respective locations. c) Histograms of SSB phase values at the same atomic sites as in b), together with Gaussian fits of the phase distribution of the structures. The violet and turquoise lines represent the distribution of the Mo and S₂ phase values, respectively. d) Relative occurrence of dopant structures obtained from large scale HAADF imaging. As Pt@V_{1S} and Pt@V_{2S} are barely distinguishable in HAADF images both types are counted together and the tip of the Pt@V_{1S+2S} column is shaded in red to mark the approximate ratio of Pt@V_{2S} based on the ratio between V_{1S} and V_{2S}. The uncertainty in the columns is based on the variation between observed images and rounded up to the next integer percentage. N is the number of cases for each histogram.

Pt atoms are stabilized by very thin carbon contamination on the MoS₂ surface.

Figures 4b and 4c show histograms of the maximum HAADF intensities and phase maxima at the same Pt-doped sites. While Pt@V_{1S} and Pt@V_{2S} distributions overlap in HAADF imaging, the phase distributions in SSB imaging are significantly more distinct. As we have only obtained a limited amount of SSB data, the distribution of different Pt dopant types plotted in Fig. 4d is based on large-scale HAADF images. Due to the poor distinguishability of Pt@V_{1S} and Pt@V_{2S} in HAADF, these are shown in the same column. Notably, the ratio between Pt atoms in S and Mo vacancies is the same as the ratio of the vacancies themselves, leading to the assumption that the Pt atoms are incorporated into the first defect they find after landing on the MoS₂ surface. Therefore we shaded the tip of the Pt@V_{1S+2S} column in Fig. 4d in red to mark the approximate ratio of Pt@V_{2S} based on the ratio between V_{1S} and V_{2S}.

Since the phase contrast is directly related to the local electron charge density, which can change depending on the chemical interactions between the atoms, using a model of non-interacting atoms is, strictly speaking, not sufficient for fully quantitative image simulations.⁴² Supplemental Material Fig. S9 contains simulated images with independent-atom-model (IAM) and DFT potentials of Pt@V_{1S} and Pt@V_{2S} structures as well as their difference. Evidently the simulated phase shifts due to charge transfer to the Pt dopant sites in MoS₂ are in the range of one percent of the absolute phase values and thus well within the range of the observed phase uncertainty in SSB. This suggests that simulations based on the IAM are precise enough for qualitative analysis in this system.

Conclusions and Outlook

In summary, by combining helium ion irradiation to create controlled vacancy defects and subsequent Pt atom incorporation via evaporation, we successfully achieved substitutional platinum doping of sulfur (V_{1S}, V_{2S}) and molybdenum (V_{Mo}) lattice sites in monolayer MoS₂.

We further demonstrate that SSB ptychography is a powerful imaging technique for reliably identifying and characterizing defect and dopant structures in Pt-doped MoS₂ monolayers at atomic resolution. The phase contrast obtained by SSB allows to reliably differentiate between various dopant and defect configurations, such as Pt atoms in single and double sulfur vacancies, which are difficult to resolve using HAADF-STEM imaging alone.

However, SSB is not without limitations: its phase contrast depends on the local atomic environment, there is a reduced Z -contrast between heavy and light elements, and further non-linearity can be introduced due to charge redistribution, introducing challenges in image interpretation. Further, the large data volumes and computational demands required for SSB make it less scalable for large-area imaging compared to HAADF-STEM.

In the future, our substitutional doping method could be further optimized by fine-tuning the ion beam parameters to increase the precision of the defect creation process. Moreover, a resulfurization step could be applied before or after Pt evaporation to repair undesired defects, thereby improving the control and uniformity in dopant placement. These refinements enhance the scalability and reproducibility of Pt doping in MoS₂, offering a promising pathway for controlled defect engineering and functionalization of materials for advanced applications in catalysis and electronics.

Supporting Information Available

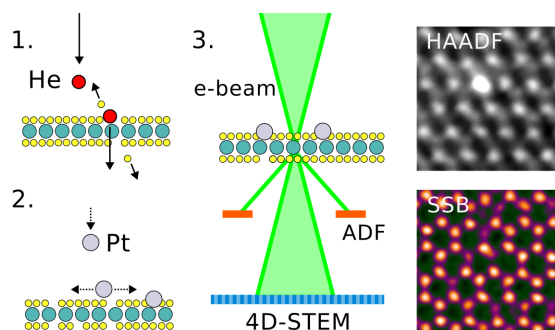
The following files are available free of charge:

- Supplementary Material: Additional information about the sample preparation and the substitutional doping method, details of the experimental imaging conditions; remarks on contamination and EELS spectra; details of the image simulation as well as information about DFT calculations; supporting figures of the implantation process and phase quantification.

Acknowledgement

We thank Neill McEvoy for kindly providing us with the MoS₂ samples used in this study as well as Yossarian Liebsch and Umair Javed for providing MoS₂ samples that were used in preparation for this study. We acknowledge funding from the Austrian Science Fund (FWF) [10.55776/P35318, 10.55776/DOC142, 10.55776/36264, 10.55776/COE5].

TOC graphic



References

- (1) Ge, J.; Zhang, D.; Qin, Y.; Dou, T.; Jiang, M.; Zhang, F.; Lei, X. Dual-metallic single Ru and Ni atoms decoration of MoS₂ for high-efficiency hydrogen production. *Applied Catalysis B: Environmental* **2021**, *298*, 120557.
- (2) Shi, Y.; Huang, J.-K.; Jin, L.; Hsu, Y.-T.; Yu, S. F.; Li, L.-J.; Yang, H. Y. Selective Decoration of Au Nanoparticles on Monolayer MoS₂ Single Crystals. *Scientific Reports* **2013**, *3*, 1839.
- (3) Wang, X.; Zhang, Y.; Si, H.; Zhang, Q.; Wu, J.; Gao, L.; Wei, X.; Sun, Y.; Liao, Q.; Zhang, Z.; Ammarah, K.; Gu, L.; Kang, Z.; Zhang, Y. Single-Atom Vacancy Defect to Trigger High-Efficiency Hydrogen Evolution of MoS₂. *Journal of the American Chemical Society* **2020**, *142*, 4298–4308.

- (4) Madauß, L. et al. Highly active single-layer MoS₂ catalysts synthesized by swift heavy ion irradiation. *Nanoscale* **2018**, *10*, 22908–22916.
- (5) Woods, J. M.; Jung, Y.; Xie, Y.; Liu, W.; Liu, Y.; Wang, H.; Cha, J. J. One-Step Synthesis of MoS₂/WS₂ Layered Heterostructures and Catalytic Activity of Defective Transition Metal Dichalcogenide Films. *ACS Nano* **2016**, *10*, 2004–2009.
- (6) Zhao, Q.; Zhou, W.; Zhang, M.; Wang, Y.; Duan, Z.; Tan, C.; Liu, B.; Ouyang, F.; Yuan, Z.; Tai, H.; Jiang, Y. Edge-Enriched Mo₂TiC₂T_x/MoS₂ Heterostructure with Coupling Interface for Selective NO₂ Monitoring. *Advanced Functional Materials* **2022**, *32*, 2203528, _eprint: <https://onlinelibrary.wiley.com/doi/pdf/10.1002/adfm.202203528>.
- (7) Filipovic, L.; Selberherr, S. Application of Two-Dimensional Materials towards CMOS-Integrated Gas Sensors. *Nanomaterials* **2022**, *12*, 3651.
- (8) Sovizi, S.; Tosoni, S.; Szoszkiewicz, R. MoS₂ oxidative etching caught in the act: formation of single (MoO₃)_n molecules. *Nanoscale Advances* **2022**, *4*, 4517–4525.
- (9) Tang, J. et al. In Situ Oxygen Doping of Monolayer MoS₂ for Novel Electronics. *Small* **2020**, *16*, 2004276, _eprint: <https://onlinelibrary.wiley.com/doi/pdf/10.1002/sml.202004276>.
- (10) Zhang, J.; Zhu, Y.; Tebyetekerwa, M.; Li, D.; Liu, D.; Lei, W.; Wang, L.; Zhang, Y.; Lu, Y. Vanadium-Doped Monolayer MoS₂ with Tunable Optical Properties for Field-Effect Transistors. *ACS Applied Nano Materials* **2021**, *4*, 769–777.
- (11) Gong, Y. et al. Band Gap Engineering and Layer-by-Layer Mapping of Selenium-Doped Molybdenum Disulfide. *Nano Letters* **2014**, *14*, 442–449.
- (12) Azcatl, A.; Qin, X.; Prakash, A.; Zhang, C.; Cheng, L.; Wang, Q.; Lu, N.; Kim, M. J.; Kim, J.; Cho, K.; Addou, R.; Hinkle, C. L.; Appenzeller, J.; Wallace, R. M. Covalent

- Nitrogen Doping and Compressive Strain in MoS₂ by Remote N₂ Plasma Exposure. *Nano Letters* **2016**, *16*, 5437–5443.
- (13) Kim, K. H.; Kim, K. S.; Ji, Y. J.; Moon, I.; Heo, K.; Kang, D.-H.; Kim, K. N.; Yoo, W. J.; Park, J.-H.; Yeom, G. Y. Effect of large work function modulation of MoS₂ by controllable chlorine doping using a remote plasma. *Journal of Materials Chemistry C* **2020**, *8*, 1846–1851.
- (14) Meng, X.; Ma, C.; Jiang, L.; Si, R.; Meng, X.; Tu, Y.; Yu, L.; Bao, X.; Deng, D. Distance Synergy of MoS₂-Confined Rhodium Atoms for Highly Efficient Hydrogen Evolution. *Angewandte Chemie* **2020**, *132*, 10588–10593, _eprint: <https://onlinelibrary.wiley.com/doi/pdf/10.1002/ange.202003484>.
- (15) Rong, J.; Ye, Y.; Cao, J.; Liu, X.; Fan, H.; Yang, S.; Wei, M.; Yang, L.; Yang, J.; Chen, Y. Restructuring electronic structure via W doped 1T MoS₂ for enhancing hydrogen evolution reaction. *Applied Surface Science* **2022**, *579*, 152216.
- (16) Li, Q. et al. Enhanced Valley Zeeman Splitting in Fe-Doped Monolayer MoS₂. *ACS Nano* **2020**, *14*, 4636–4645.
- (17) Li, M.; Wu, X.; Guo, W.; Liu, Y.; Xiao, C.; Ou, T.; Zheng, Y.; Wang, Y. Controllable p-type doping of monolayer MoS₂ with tantalum by one-step chemical vapor deposition. *Journal of Materials Chemistry C* **2022**, *10*, 7662–7673.
- (18) Liu, X.; Chen, J.; Hu, Y.; Pan, Q.; Zhong, H.; Zeng, R.; Shao, T.; He, Z.; Chen, J.; Chen, J. Optimization of the in-plane activity of MoS₂ monolayer by Pd-S bonds for hydrogen evolution reaction. *Applied Surface Science* **2024**, *642*, 158563.
- (19) Burman, D.; Raha, H.; Manna, B.; Pramanik, P.; Guha, P. K. Substitutional Doping of MoS₂ for Superior Gas-Sensing Applications: A Proof of Concept. *ACS Sensors* **2021**, *6*, 3398–3408.

- (20) Li, Y.; Gu, Q.; Johannessen, B.; Zheng, Z.; Li, C.; Luo, Y.; Zhang, Z.; Zhang, Q.; Fan, H.; Luo, W.; Liu, B.; Dou, S.; Liu, H. Synergistic Pt doping and phase conversion engineering in two-dimensional MoS₂ for efficient hydrogen evolution. *Nano Energy* **2021**, *84*, 105898.
- (21) Li, H.; Wang, S.; Sawada, H.; Han, G. G. D.; Samuels, T.; Allen, C. S.; Kirkland, A. I.; Grossman, J. C.; Warner, J. H. Atomic Structure and Dynamics of Single Platinum Atom Interactions with Monolayer MoS₂. *ACS Nano* **2017**, *11*, 3392–3403.
- (22) Li, H.; Wang, L.; Dai, Y.; Pu, Z.; Lao, Z.; Chen, Y.; Wang, M.; Zheng, X.; Zhu, J.; Zhang, W.; Si, R.; Ma, C.; Zeng, J. Synergetic interaction between neighbouring platinum monomers in CO₂ hydrogenation. *Nature Nanotechnology* **2018**, *13*, 411–417.
- (23) Shi, Z. et al. Phase-dependent growth of Pt on MoS₂ for highly efficient H₂ evolution. *Nature* **2023**, *621*, 300–305.
- (24) Trentino, A.; Zagler, G.; Längle, M.; Madsen, J.; Susi, T.; Mangler, C.; Åhlgren, E. H.; Mustonen, K.; Kotakoski, J. Single atoms and metal nanoclusters anchored to graphene vacancies. *Micron* **2024**, *184*, 103667.
- (25) Trentino, A.; Mizohata, K.; Zagler, G.; Längle, M.; Mustonen, K.; Susi, T.; Kotakoski, J.; Åhlgren, E. H. Two-step implantation of gold into graphene. *2D Materials* **2022**, *9*, 025011.
- (26) Zagler, G.; Stecher, M.; Trentino, A.; Kraft, F.; Su, C.; Postl, A.; Längle, M.; Pesenhofer, C.; Mangler, C.; Åhlgren, E. H.; Markevich, A.; Zettl, A.; Kotakoski, J.; Susi, T.; Mustonen, K. Beam-driven dynamics of aluminium dopants in graphene. *2D Materials* **2022**, *9*, 035009.
- (27) Pennycook, T. J.; Lupini, A. R.; Yang, H.; Murfitt, M. F.; Jones, L.; Nellist, P. D. Efficient phase contrast imaging in STEM using a pixelated detector. Part 1: experimental demonstration at atomic resolution. *Ultramicroscopy* **2015**, *151*, 160–167.

- (28) Krivanek, O. L.; Chisholm, M. F.; Nicolosi, V.; Pennycook, T. J.; Corbin, G. J.; Dellby, N.; Murfitt, M. F.; Own, C. S.; Szilagy, Z. S.; Oxley, M. P.; Pantelides, S. T.; Pennycook, S. J. Atom-by-atom structural and chemical analysis by annular dark-field electron microscopy. *Nature* **2010**, *464*, 571–574.
- (29) Yücelen, E.; Lazić, I.; Bosch, E. G. T. Phase contrast scanning transmission electron microscopy imaging of light and heavy atoms at the limit of contrast and resolution. *Scientific Reports* **2018**, *8*, 2676.
- (30) Wen, Y.; Ophus, C.; Allen, C. S.; Fang, S.; Chen, J.; Kaxiras, E.; Kirkland, A. I.; Warner, J. H. Simultaneous Identification of Low and High Atomic Number Atoms in Monolayer 2D Materials Using 4D Scanning Transmission Electron Microscopy. *Nano Letters* **2019**, *19*, 6482–6491.
- (31) Mangler, C.; Meyer, J.; Mittelberger, A.; Mustonen, K.; Susi, T.; Kotakoski, J. A Materials Scientist’s CANVAS: A System for Controlled Alteration of Nanomaterials in Vacuum Down to the Atomic Scale. *Microscopy and Microanalysis* **2022**, *28*, 2940–2942.
- (32) Komsa, H.-P.; Kotakoski, J.; Kurasch, S.; Lehtinen, O.; Kaiser, U.; Krasheninikov, A. V. Two-Dimensional Transition Metal Dichalcogenides under Electron Irradiation: Defect Production and Doping. *Physical Review Letters* **2012**, *109*, 035503.
- (33) Yoshimura, A.; Lamparski, M.; Giedt, J.; Lingerfelt, D.; Jakowski, J.; Ganesh, P.; Yu, T.; Sumpter, B. G.; Meunier, V. Quantum theory of electronic excitation and sputtering by transmission electron microscopy. *Nanoscale* **2023**, *15*, 1053–1067.
- (34) Madsen, J.; Susi, T. The abTEM code: transmission electron microscopy from first principles. *Open Research Europe* **2021**, *1*, 24.
- (35) Jiang, Y.; Chen, Z.; Han, Y.; Deb, P.; Gao, H.; Xie, S.; Purohit, P.; Tate, M. W.;

- Park, J.; Gruner, S. M.; Elser, V.; Muller, D. A. Electron ptychography of 2D materials to deep sub-ångström resolution. *Nature* **2018**, *559*, 343–349.
- (36) Ghorbani-Asl, M.; Kretschmer, S.; Spearot, D. E.; Krasheninnikov, A. V. Two-dimensional MoS₂ under ion irradiation: from controlled defect production to electronic structure engineering. *2D Materials* **2017**, *4*, 025078.
- (37) Hofer, C.; Pennycook, T. J. Reliable phase quantification in focused probe electron ptychography of thin materials. *Ultramicroscopy* **2023**, *254*, 113829.
- (38) Wen, Y. Structural study of two-dimensional semiconductors using four-dimensional scanning transmission electron microscopy. Ph.D. thesis, University of Oxford, 2021; PhD Thesis, <https://www.ora.ox.ac.uk/objects/uuid:908de875-85b4-41e7-90cf-16f68ab28b8b>.
- (39) Wang, S.; Lee, G.-D.; Lee, S.; Yoon, E.; Warner, J. H. Detailed Atomic Reconstruction of Extended Line Defects in Monolayer MoS₂. *ACS Nano* **2016**, *10*, 5419–5430.
- (40) Park, Y.; Li, N.; Jung, D.; Singh, L. T.; Baik, J.; Lee, E.; Oh, D.; Kim, Y. D.; Lee, J. Y.; Woo, J.; Park, S.; Kim, H.; Lee, G.; Lee, G.; Hwang, C.-C. Unveiling the origin of n-type doping of natural MoS₂: carbon. *npj 2D Materials and Applications* **2023**, *7*, 1–7.
- (41) Farigliano, L. M.; Paredes-Olivera, P. A.; Patrito, E. M. Initial Steps of Oxidative Etching of MoS₂ Basal Plane Induced by O₂. *The Journal of Physical Chemistry C* **2020**, *124*, 13177–13186.
- (42) Madsen, J.; Pennycook, T. J.; Susi, T. *ab initio* description of bonding for transmission electron microscopy. *Ultramicroscopy* **2021**, *231*, 113253.
- (43) O’Brien, M.; McEvoy, N.; Hallam, T.; Kim, H.-Y.; Berner, N. C.; Hanlon, D.; Lee, K.;

- Coleman, J. N.; Duesberg, G. S. Transition Metal Dichalcogenide Growth via Close Proximity Precursor Supply. *Scientific Reports* **2014**, *4*, 7374.
- (44) Meyer, J. C.; Girit, C. O.; Crommie, M. F.; Zettl, A. Hydrocarbon lithography on graphene membranes. *Applied Physics Letters* **2008**, *92*, 123110.
- (45) Susi, T.; Hardcastle, T. P.; Hofsäss, H.; Mittelberger, A.; Pennycook, T. J.; Mangler, C.; Drummond-Brydson, R.; Scott, A. J.; Meyer, J. C.; Kotakoski, J. Single-atom spectroscopy of phosphorus dopants implanted into graphene. *2D Materials* **2017**, *4*, 021013.
- (46) Susi, T.; Dellby, N.; Hayner, R.; Hofer, C.; Kotakoski, J.; Lovejoy, T. C.; Mangler, C.; Mittelberger, A.; Pennycook, T. J.; Plotkin-Swing, B. Open-Source Phase Reconstructions of Focused-Probe 4D-STEM Data with Near-Ideal Direct-Electron Detection. *Microscopy and Microanalysis* **2024**, *30*, ozae044.920.
- (47) Hofer, C.; Madsen, J.; Susi, T.; Pennycook, T. J. Detecting charge transfer at defects in 2D materials with electron ptychography. 2023; <https://arxiv.org/abs/2301.04469v4>, arXiv:2301.04469v4 [cond-mat.mtrl-sci].
- (48) Kühne, T. D. et al. CP2K: An electronic structure and molecular dynamics software package - Quickstep: Efficient and accurate electronic structure calculations. *The Journal of Chemical Physics* **2020**, *152*, 194103.
- (49) Goedecker, S.; Teter, M.; Hutter, J. Separable dual-space Gaussian pseudopotentials. *Physical Review B* **1996**, *54*, 1703–1710.
- (50) Perdew, J. P.; Burke, K.; Ernzerhof, M. Generalized Gradient Approximation Made Simple. *Physical Review Letters* **1996**, *77*, 3865–3868.
- (51) Henkelman, G.; Uberuaga, B. P.; Jónsson, H. A climbing image nudged elastic band

- method for finding saddle points and minimum energy paths. *The Journal of Chemical Physics* **2000**, *113*, 9901–9904.
- (52) Mannebach, E. M. et al. Dynamic Structural Response and Deformations of Monolayer MoS₂ Visualized by Femtosecond Electron Diffraction. *Nano Letters* **2015**, *15*, 6889–6895.
- (53) Susi, T.; Madsen, J.; Ludacka, U.; Mortensen, J. J.; Pennycook, T. J.; Lee, Z.; Kotakoski, J.; Kaiser, U.; Meyer, J. C. Efficient first principles simulation of electron scattering factors for transmission electron microscopy. *Ultramicroscopy* **2019**, *197*, 16–22.
- (54) Längle, M.; Mayer, B. M.; Madsen, J.; Propst, D.; Bo, A.; Kofler, C.; Hana, V.; Mangler, C.; Susi, T.; Kotakoski, J. Defect-engineering hexagonal boron nitride using low-energy Ar⁺ irradiation. 2024; <http://arxiv.org/abs/2404.07166>, arXiv:2404.07166 [cond-mat].
- (55) Komsa, H.-P.; Kurasch, S.; Lehtinen, O.; Kaiser, U.; Krasheninnikov, A. V. From point to extended defects in two-dimensional MoS₂: Evolution of atomic structure under electron irradiation. *Physical Review B* **2013**, *88*, 035301.
- (56) Peña, F. d. l. et al. hyperspy/hyperspy: v2.2.0. 2024; <https://zenodo.org/records/14057415>.
- (57) Campos-Roldán, C. A.; Chattot, R.; Filhol, J.-S.; Guesmi, H.; Pailloux, F.; Bacabe, R.; Blanchard, P.-Y.; Zitolo, A.; Drnec, J.; Jones, D. J.; Cavaliere, S. Structure Dynamics of Carbon-Supported Platinum-Neodymium Nanoalloys during the Oxygen Reduction Reaction. *ACS Catalysis* **2023**, *13*, 7417–7427.

Supplementary Material

Methods

Sample preparation The MoS₂ sample was grown on SiO₂ via chemical vapor deposition (CVD)⁴³ using liquid-phase exfoliated MoO₃ as precursor and consists of mostly triangular monolayered flakes with an edge lengths between 5 and 20 μm . The samples were subsequently transferred in air onto a gold transmission electron microscopy grid with a holey membrane of amorphous carbon (Quantifoil R 1.2/1.3 Au grid) using the method described in.⁴⁴

Substitutional doping with single Pt atoms After transferring to the TEM grid, the MoS₂ samples were introduced into the interconnected near-UHV CANVAS system³¹ (base pressure of 10^{-8} mbar), which features both a SPECS ECR-HO microwave plasma generator and evaporation sources. Low-energy He ions from the plasma generator with a current of ca. 2.5 nA were used to irradiate the MoS₂ samples. The measured ion energy for these parameters is approximately normally distributed with a mean of ca. 170 eV and a standard deviation of ca. 20 eV. Irradiation for 10 min corresponds to a fluence of ca. 1.25×10^{13} cm⁻². The plasma treatment was followed by evaporation of the platinum. For Pt, the tip of a 99.9% Pt rod was heated up with an EFM-3 e-beam evaporator using a filament current of 2.9 A and an extraction voltage of 1850 V to produce a Pt flux of ca. 0.6 nA. After 10 min of evaporation, single Pt atoms were found in the MoS₂ lattice.

Microscopy and spectroscopy After implantation, the samples were transferred inside the UHV system to the aberration-corrected Nion UltraSTEM100 scanning transmission electron microscope operated at 60 kV acceleration voltage. Images were acquired using a HAADF detector with a probe convergence semi-angle of ca. 35 mrad and a semi-angular range of 80–300 mrad. HAADF images with 2048 \times 2048 pixels were further processed using Gaussian blurring in order to reduce noise and increase contrast of the images. EEL spectra were recorded with a Gatan PEELS 666 spectrometer with an Andor iXon 897 CCD camera

and an energy-dispersion of 0.5 eV/pixel.⁴⁵ For 4D data collection, stacks with 512×512 real-space pixels were collected using a Dectris ARINA direct-electron detector with a dwell time of 20 μs and an average dose of ca. $1 \times 10^5 \text{ e}^-/\text{Å}^2$. To reduce the size of the data, recorded at each imaged position (which can be up to 10 GB for a single dataset), we reduced the size of the convergent-beam electron diffraction patterns recorded at each probe position to 48×48 pixels by binning, which only has a negligent influence on the quality of the reconstructed phase.⁴⁶ SSB ptychography was performed with the open-source PyPtychoSTEM package,⁴⁷ using the experimental 4D-STEM data as input. The convergence angle was set to 35 mrad and the step size was 0.156 Å per pixel (matched in the SSB reconstruction). Post-collection aberration correction was applied using singular value decomposition to identify the residual aberrations which were then counteracted.

Density functional theory To determine the minimum energy paths and transition states for several possible diffusion events on the MoS₂ monolayer, a density functional theory (DFT) based *ab initio* simulation approach as implemented in the CP2K⁴⁸ code (version 2023.2) was used. For all calculations the norm-conserving, separable, dual-space Gaussian-type pseudopotentials of Goedecker, Teter, and Hutter (GTH)⁴⁹ were used with a 500 Ry plane wave cutoff of the multigrid. The exchange-correlation interactions were treated with the Perdew–Burke–Ernzerhof (PBE)⁵⁰ generalized gradient approximation. As a basis for all calculations, $5 \times 5 \times 1$ MoS₂ monolayer supercells was used consisting of 75 atoms with a vacuum layer of 40 Å in order to prevent artificial interactions between periodic images. After a cell relaxation of the pristine material, the supercells were modified in order to determine the minimum energy paths for diffusion of Pt and S atoms on the surface of (defective) MoS₂. For this, the climbing image nudged elastic band method⁵¹ was used with 12 images and a maximum force convergence criteria of 0.01 Hartree per Bohr.

HAADF and 4D-STEM image simulations HAADF-STEM image simulations were performed based on the DFT-relaxed models using the *abTEM* package.³⁴ Similar to the experiment, the HAADF detector semi-angular ranges was set to 80–300 mrad and the probe

convergence angle was set to 35 mrad. For all simulations an electron beam energy of 60 keV was assumed. To account for thermal diffuse scattering, we implemented the frozen-phonon model with 20 snapshots per image using standard deviation of atomic displacements values taken from.⁵² For 4D-STEM the same parameters were used, but instead of the HAADF detector a pixelated detector setting was used. After creating the artificial 4D-STEM data, the phase images were reconstructed using the same algorithm and parameters as in the corresponding experimental images, including the dose per area simulated by adding Poisson noise to the diffraction patterns. To account for finite probe-size effects in SSB images, we added a Gaussian blur over the simulated images to match the line profile of the experimental SSB data. For the charge-transfer simulations, the DFT potential was calculated from the all-electron charge density converged with GPAW, as described in.⁵³

Optimization method for phase quantification The phase information of experimental and simulated phase images was retrieved by an SSB contrast transfer function (CTF) based kernel.³⁷ First, an initial atomic model corresponding to the input phase image is created. Using the initial model, a phase image is simulated, convolving the point potential of the model with the inverse Fourier transform of the CTF. Then, the simulated image is matched to the input image by iteratively updating the free parameters of the simulated image, such that the difference between the simulated image and the input image is minimized. Parameters that can be optimized are positions and intensities of the atoms, scale and lateral translation of the atomic model, aberrations (up to the third order), sample tilt, and blur. Note that the model optimizes the phase shifts due to each atom, even when more than one is located at the same atom column. To achieve a more reliable phase match, we limited the amount of free parameters in some iteration steps, effectively adding new parameters after a certain amount of iterations. Correlations between the optimized images and the experimental data were above 95 % for all images.

Evaporation of Pt on graphene and EELS measurements Commercial graphene grown via CVD provided on a sacrificial polymethyl methacrylate (PMMA) layer (Easy

Transfer graphene) was transferred onto a SiN TEM grid with with 3 μm holes (Silson Ltd) via a liquid transfer method using deionized water as the carrier liquid. Following the transfer onto the substrate the graphene was heated on a hot plate at 150°C for 1 h. The PMMA sacrificial layer was then removed via an acetone bath at 50°C for 1 h, after which the grid rested in isopropyl alcohol (IPA) at room temperature for another hour. Graphene samples were cleaned using a 6 W continuous wave diode laser with a wavelength of 445 nm with a spot size of 0.3 \times 1.5 mm² as described in.²⁵ The surface was illuminated at 27% of the maximum power for 6 min multiple times, where the power was set by changing the duty cycle. With these parameters, not all of the surface contamination is removed, but large-enough atomically clean patches are created for acquiring statistically meaningful data. Pt was then evaporated onto the sample for 15 minutes with a flux of 0.25 nA.

Remarks on contamination

A significant number of the evaporated metal atoms can also be found on or next to hydrocarbon contamination (brighter, diffuse contrast on the image). Most of these atoms are still isolated and perhaps form chemical bonds with the hydrocarbons,²¹ but are not incorporated into the lattice.

As is evident from the images in Fig 1d-f, ion irradiation and metal evaporation lead to a slight increase in undesired hydrocarbon contamination of the sample, effectively covering vacancy sites and incorporated metals. The same can be expected for exposure of the defective MoS₂ surface to ambient conditions during sample transfer. To allow efficient implantation of dopants, protecting the sample from ambient between the steps is therefore crucial for the procedure. Nevertheless, even in UHV, every modification step can create additional contamination. Contamination during evaporation can be minimized by heat-treating the Pt source and cleaning the modification chamber with O₂ plasma (see Supplementary Material, Fig. S2).

EELS spectra of the evaporated material

Even though the high Z -contrast of the dopant atoms in HAADF-STEM and the excellent agreement with SSB image simulations are strong evidence for the element of the implanted atoms, definitive proof of the implantation of Pt atoms could benefit from additional spectroscopic evidence. Unfortunately, we were not able to obtain single-atom electron-energy loss (EEL) spectra of the Pt O_2 edge (the only Pt edge accessible to our EEL spectrometer) due to the limited stability of the MoS₂ under the electron beam and the low cross section of the Pt edge. Nevertheless, to provide spectroscopic evidence of the evaporated material, we evaporated Pt atoms onto graphene using the same setup and similar parameters. Supplementary Material Fig. S10 shows EEL spectra of a small Pt cluster formed in the graphene lattice, unambiguously demonstrating the presence of Pt.

Author contributions

DL, JK and LF conceived the study. DL and ML conducted the experimental work, TS provided code for ptychography and phase quantification and DL, ML, TS, JK and LF performed the data analysis. AB and MC performed the *ab initio* calculations. DL, JK, ML and LF wrote the manuscript, with contributions from all other authors. LF and JK supervised the study.

Supplementary Figures

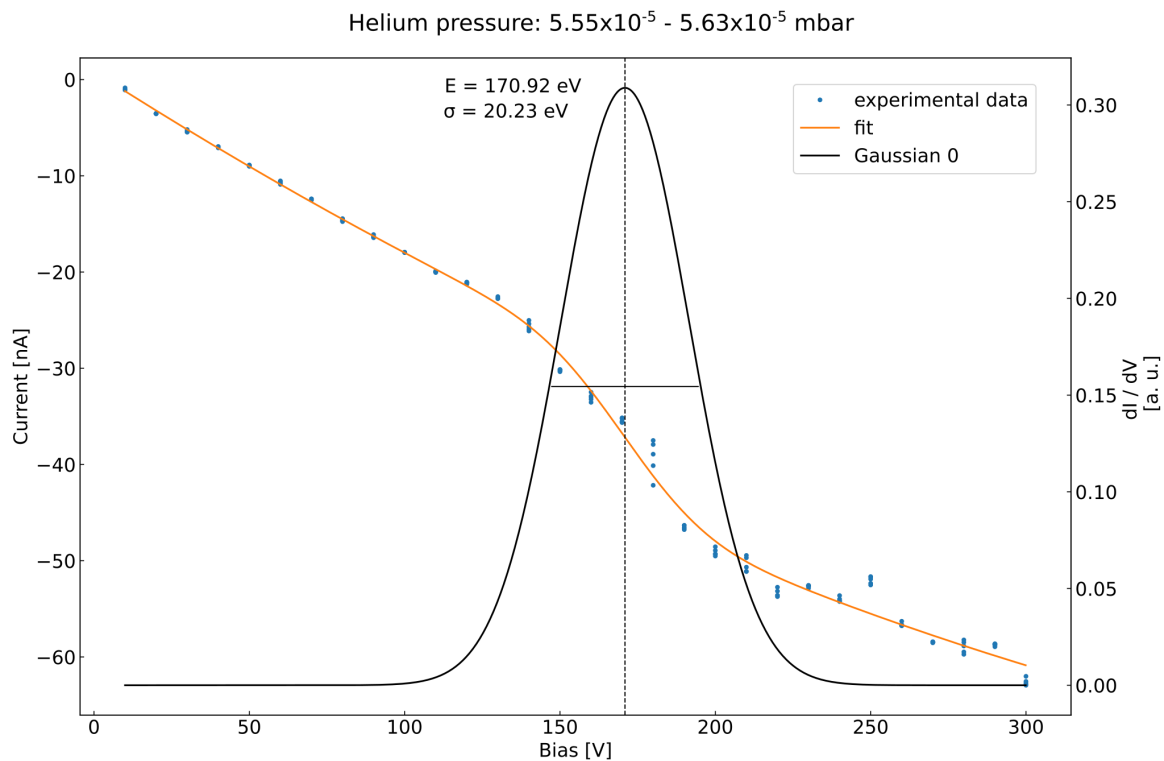


Figure S1: Beam profile and dI/dV curve of the deceleration measurement of the ion plasma. The experimental details of this analysis can be found in. ⁵⁴

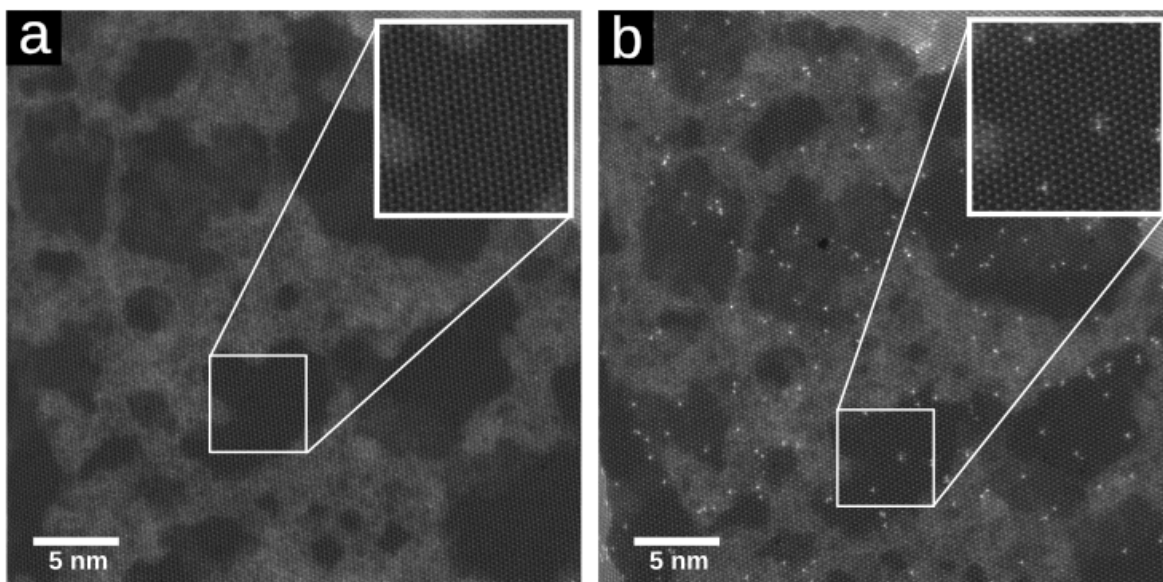


Figure S2: a) HAADF-STEM image of the pristine MoS_2 surface before evaporation b) HAADF-STEM image of the same area after evaporation of single Pt atoms.

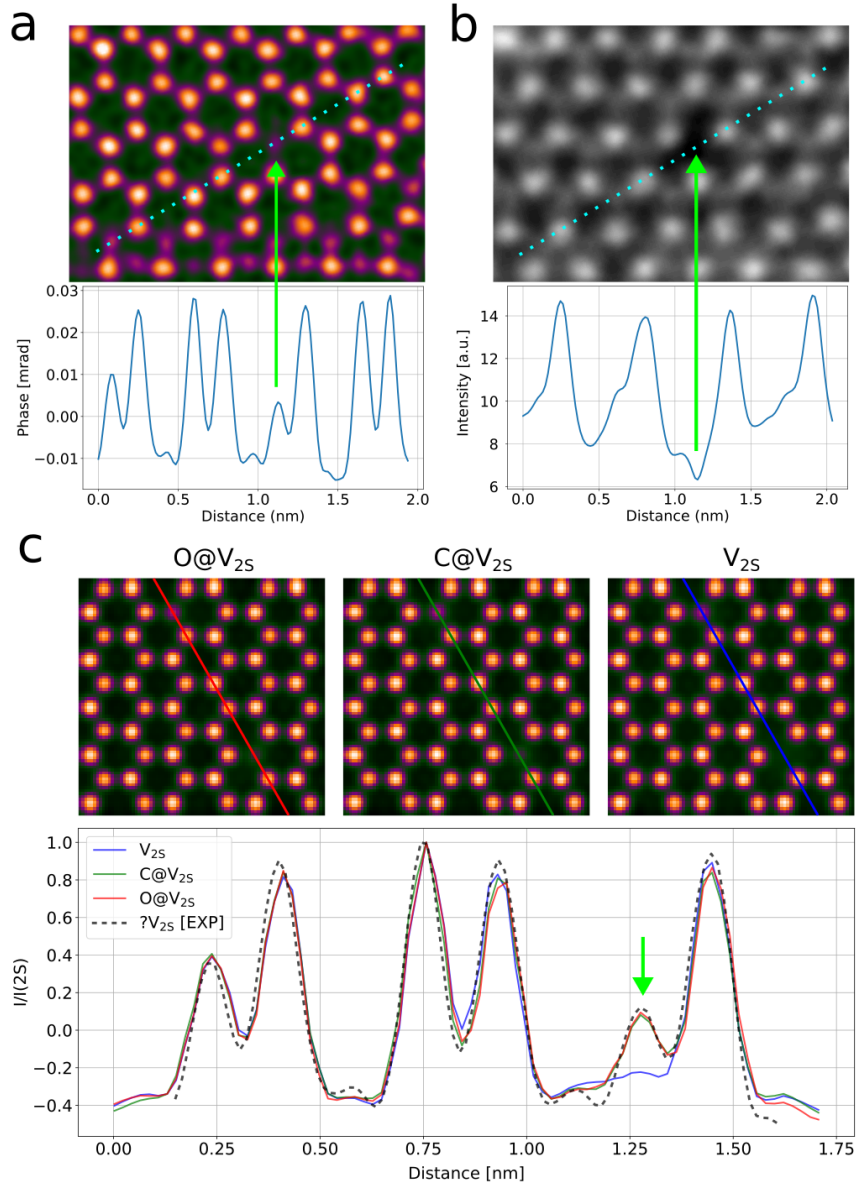


Figure S3: a) SSB phase image of highly defective MoS₂ next to a single vacancy defect line similar to the one reported in Ref.⁵⁵ The line profile over a V_{1S} and a V_{2S} is horizontally matched with the image. The unexpected local maximum at the V_{2S} is marked with a green arrow. b) Gaussian blurred HAADF-STEM image of the same structure with horizontally matched line profile. The HAADF-STEM contrast has a minimum exactly at the location of the V_{2S} (green arrow). c) Simulated SSB phase images of V_{2S} without heteroatoms, with a C dopant, and a O dopant. The plot below contains line profiles of the simulated structures and the experimental data from panel a. The location of the questionable V_{2S} site is marked with a green arrow in the line profile.

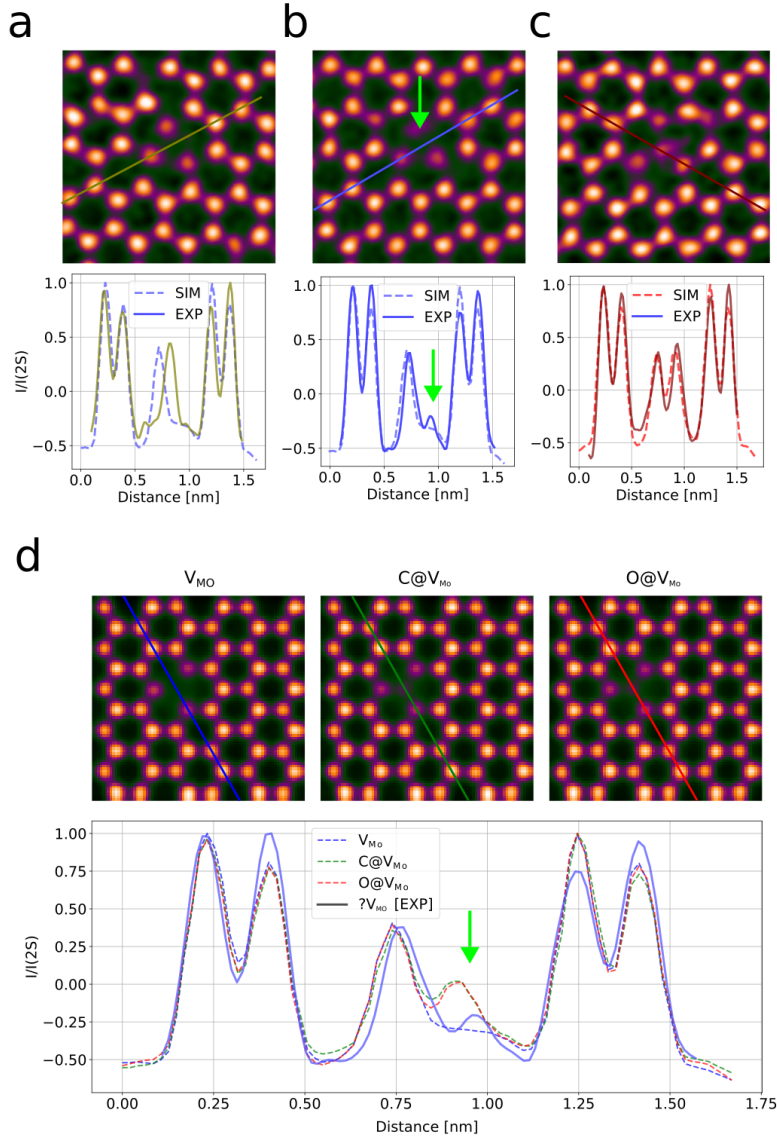


Figure S4: a) SSB phase image of a defect cluster with three S atoms missing around a V_{Mo} site. The simulated line profile corresponds to the first image in d. b) SSB phase of a similar defect cluster as in a. The simulated line profile corresponds to the first image in panel d. The unexpected local maximum at the V_{Mo} is marked with a green arrow. c) SSB image of a defect cluster with a S atom replacing the Mo atom. The simulated line profile corresponds to the third image in panel d. d) Simulated SSB phase images of V_{Mo} surrounded by three V_{IS} without heteroatoms, with a C dopant and S dopant. The plot below contains line profiles of the simulated structures and the experimental data from panel b. The location of the questionable V_{Mo} site is marked with a green arrow in the line profile.

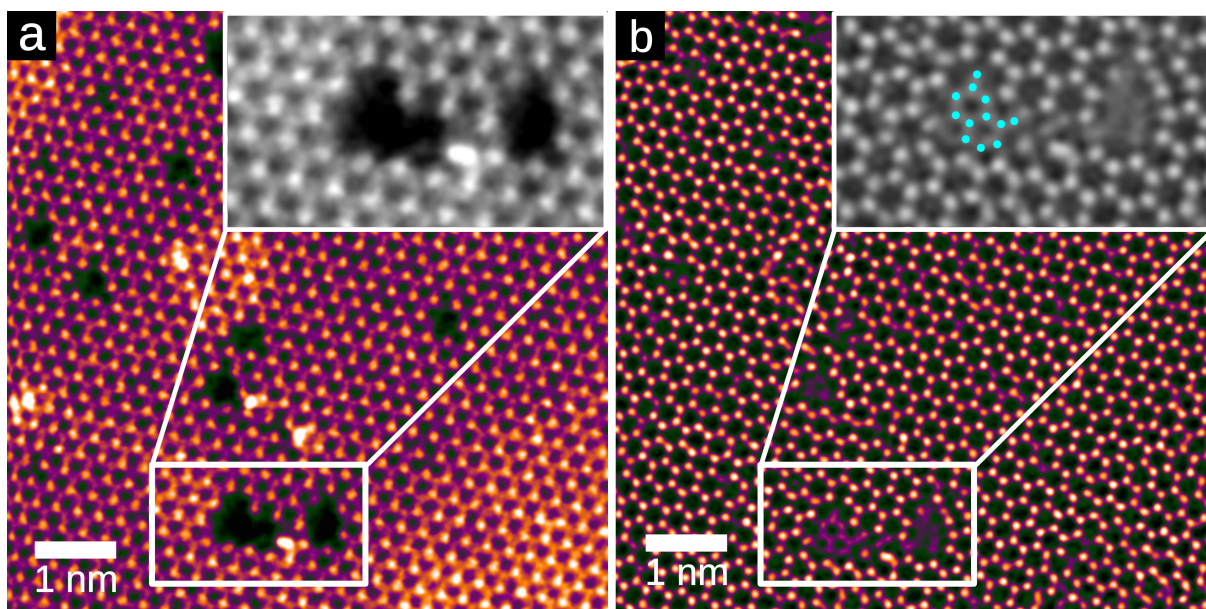


Figure S5: a) HAADF-STEM image of a defect cluster on contaminated MoS₂. b) SSB phase image of the same area: inside the defect cluster a hexagonal ring of sp² hybridized carbon is clearly visible. The approximate positions of the carbon atoms in the defect cluster are marked in the inset with cyan dots.

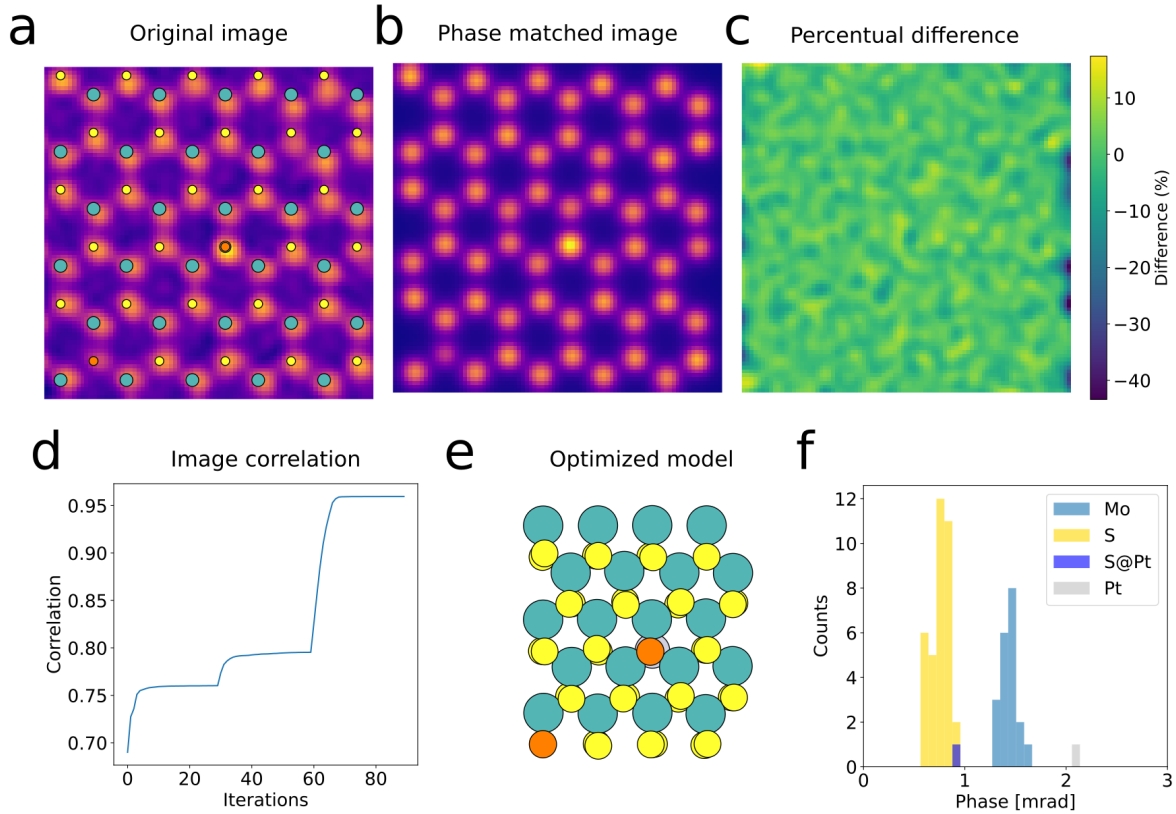


Figure S6: a) Experimental phase image of a Pt@V₂S site with the initial approximate atomic model overlaid. b) Simulated image after phase optimization. c) Relative difference between a and b (in percent). d) Correlation between a and b as a function of iterations. The first 30 iterations optimize field of view, lateral translation, image blur and tilt. The next 30 iterations additionally optimize intensities and residual aberrations (up to second order). The last 30 iterations additionally optimize the atomic positions. e) Final atomic model after optimization. As the kernel does not provide accurate quantification for atoms near to the edge of the image, we excluded the outermost atoms. f) Phase distribution of the atoms depicted in panel e. The average phase of the S atoms is 0.82 mrad, of the Mo atoms 1.36 mrad, and the phase of the Pt atom is 2.12 mrad. This leads to a $(2 \times S)/\text{Mo}$ phase ratio of 1.21. Adding the phase value of 0.91 mrad of the S atom at the Pt site to the Pt phase value leads to a $(\text{Pt}+S)/\text{Mo}$ phase ratio of 2.23 (theoretical ratio 2.23).

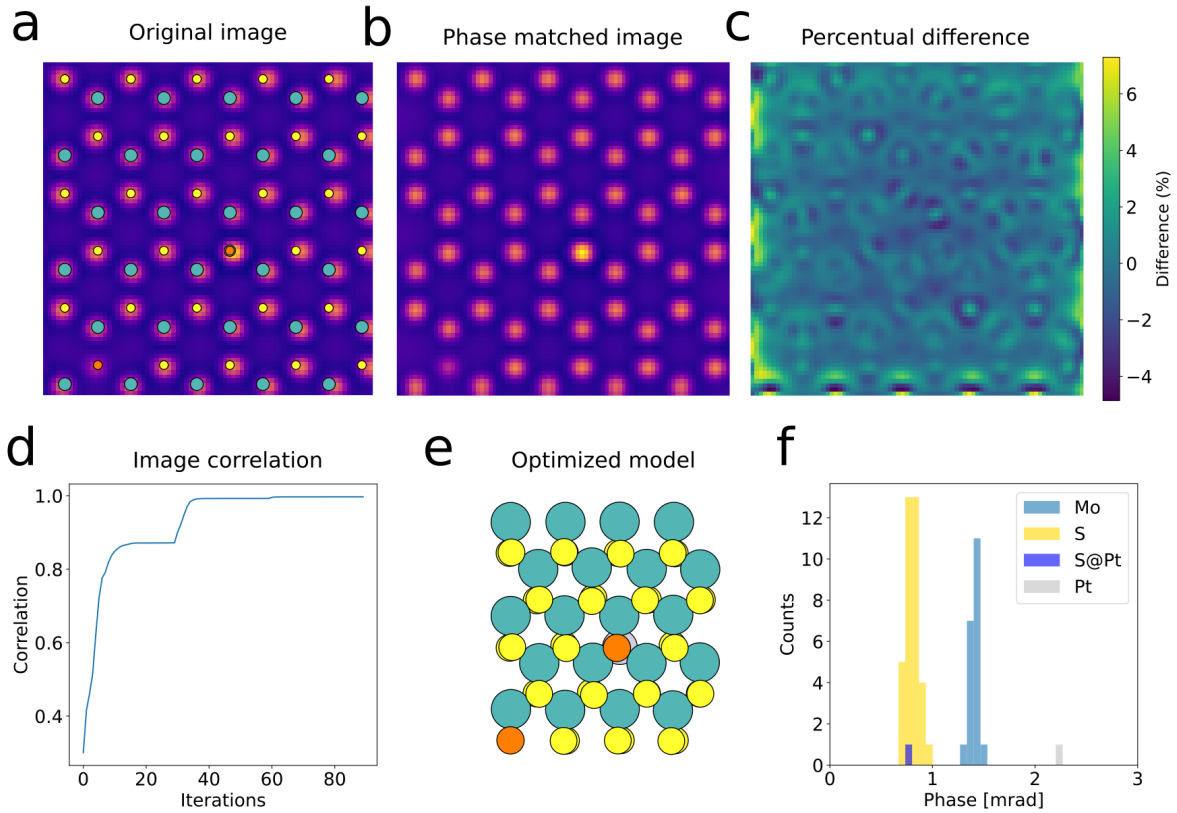


Figure S7: a) Simulated phase image of the same structure as in Fig. S6 with the initial approximate atomic model overlaid. b) Simulated image after optimization. c) Relative difference between a and b (in percentage). d) Correlation between a and b as a function of iterations. e) Final atomic model after optimization (outermost atoms excluded). f) Phase distribution of the atoms depicted in panel e. The average phase of the S atoms is 0.82 mrad, of the Mo atoms 1.39 mrad, and the phase of the Pt atom is 2.225 mrad. This leads to a $(2 \times S)/Mo$ phase ratio of 1.18. Adding the phase value of 0.65 mrad of the S atom at the Pt site to the Pt phase value leads to a $(Pt+S)/Mo$ phase ratio of 2.08 (theoretical ratio 2.23).

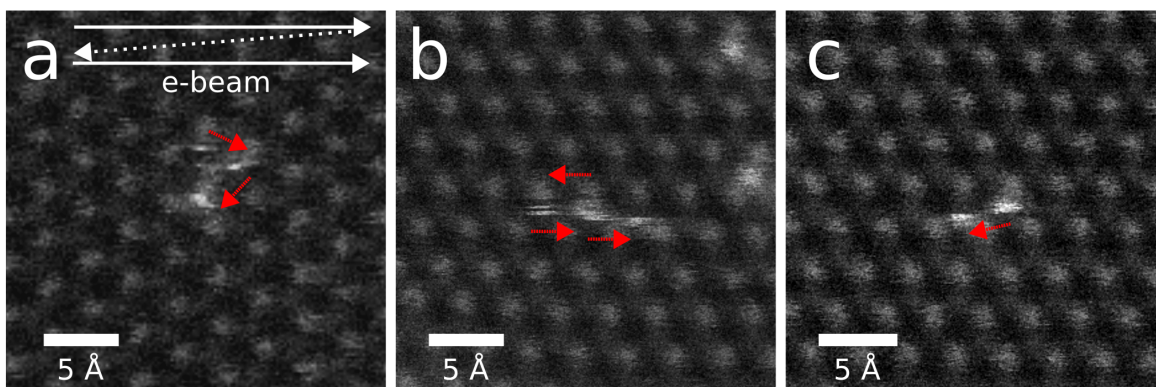


Figure S8: a-c) HAADF-STEM images of Pt atoms that are kicked out of their position by the electron beam and imaged at different locations within the same frame. The trajectory of the Pt atoms is marked in red. The direction of the scanning electron beam (white lines) is overlaid in panel a).

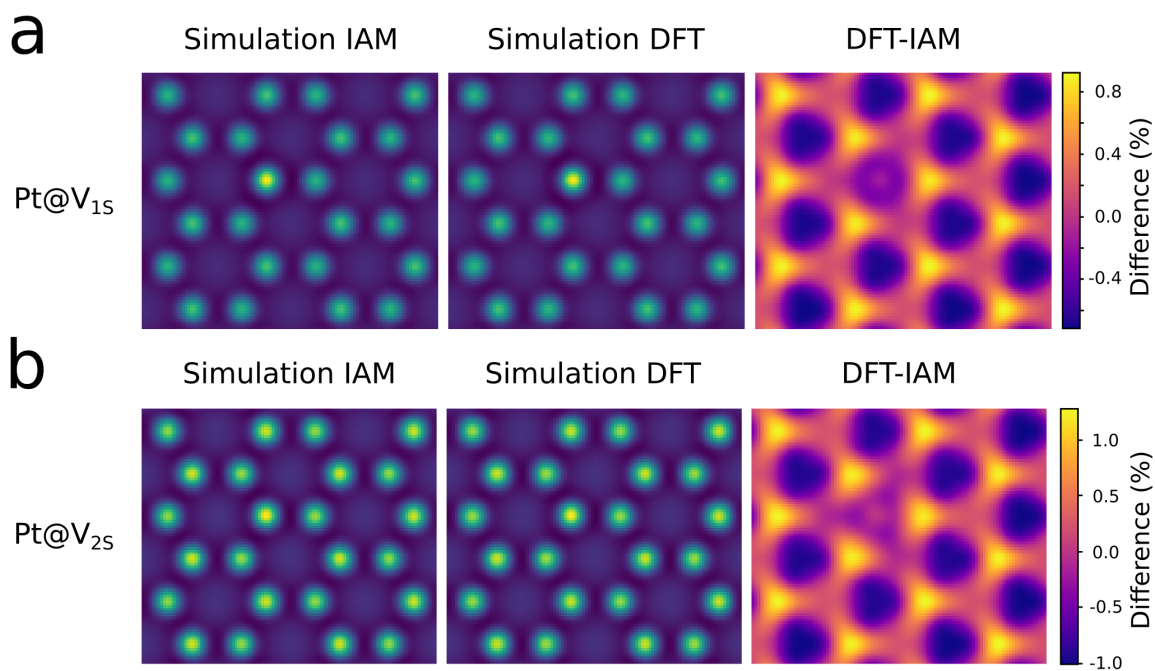


Figure S9: Phase image simulations of structures with potentials based on IAM and DFT as well as their difference for a) Pt@V_{1S} and b) Pt@V_{2S}.

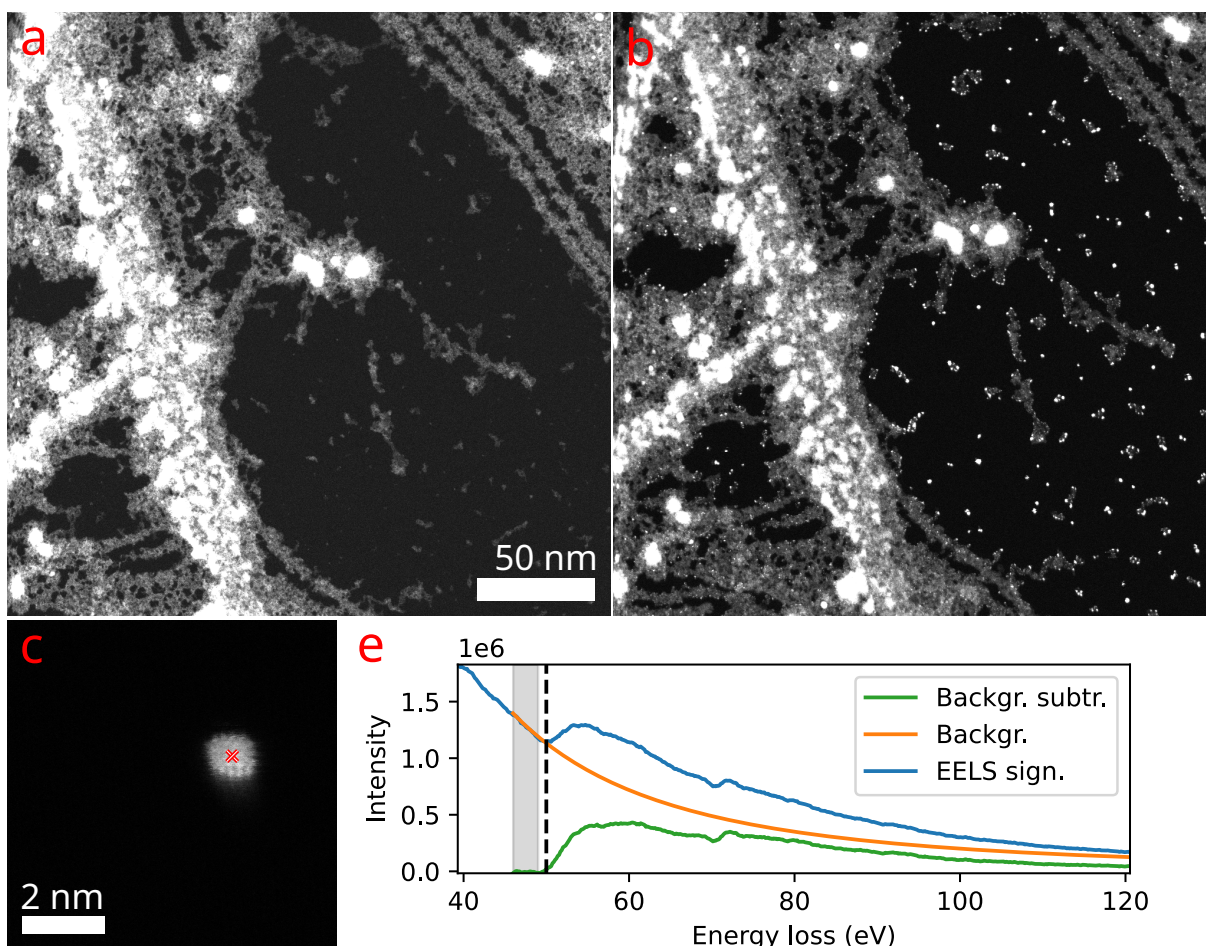


Figure S10: a) Overview HAADF-STEM image of laser-cleaned graphene. b) Overview HAADF-STEM image of the same area after Pt evaporation with an e-beam evaporator (flux: 0.25 nA, time: 15 min). c) Smaller field of view HAADF-STEM image of Pt cluster on graphene with the position of the EEL spectrum (shown in d) marked with a red cross. d) EEL spectrum recorded at the position of the red cross in panel c. The signal of the Pt cluster is shown in blue, with the background in orange and the background-subtracted spectrum in green. A power law is fitted to the original spectrum in the range of 46.0 to 49.0 eV (gray area). A black marker is positioned at an energy-loss of 50 eV. This corresponds to the Pt $O_{2,3}$ - and Pt $N_{4,6}$ -edges. Spectral analysis was done using hyperSpy.⁵⁶ The peaks align with reference spectra (EELS Atlas, <https://eels.info/atlas/platinum>). This also agrees closely with the spectrum shown in the Supplementary Figure S23 of⁵⁷